Earth, Planets and Space
a SpringerOpen Journal

LETTER Open Access

Three-dimensional magnetotelluric imaging of crustal fluids and seismicity around Naruko volcano, NE Japan

Yasuo Ogawa[1*], Masahiro Ichiki[2], Wataru Kanda[1], Masaaki Mishina[2] and Koichi Asamori[3]

Abstract

We analyzed the 3-D resistivity structure beneath Naruko volcano, northeastern Japan, with the aim of imaging 3-D distribution of fluids in the crust for its volcanic and seismogenic implications. The data were recorded at 77 sites in total: 30 sites are new and are arranged in an approximately 5 × 5 km grid whereas the remaining older sites constitute two separate east-west profiles. We ran a 3-D inversion using full components of impedance tensors in the period range between 0.13 and 400 s. The resulting model showed that a sub-vertical conductor exists a few kilometers below Naruko volcano. The conductor extends from the surface of the volcano and dips towards the south, away from the volcano towards the backbone range. High levels of seismicity are observed in the upper crust above and around the conductors. We suggest that the seismicity is fluid driven and that a fluid trap is created by the precipitation of quartz owing to a reduction in solubility at shallow depth. The Quaternary volcanic front is characterized by a sharp resistivity contrast and a high-resistivity zone and extends 10 to 15 km towards the east. A fore-arc conductor was observed at mid-crustal levels even farther towards the east. The sub-vertical conductors along the arc and the fore-arc conductor have resistivities of 1 to 10 Ωm. Assuming a Hashin-Shtrikman model with saline fluids of 0.1-Ωm resistivity, a porosity of 1.5% to 15% is required to explain the observed conductive anomalies.

Keywords: Magnetotellurics; 3-D modeling; Saline fluids; Northeastern Japan; Quaternary volcanoes; Seismicity

Findings

Introduction

The magnetotelluric (MT) method involves the measurement of time-varying natural electromagnetic fields for the remote detection of small volumes of fluid or melt in the crust and upper mantle (e.g., Hill et al. 2009; Wannamaker et al. 2009; Ingham et al. 2009; Aizawa et al. 2014). The bulk resistivity of the fluid- or melt-bearing rock is not controlled by the resistivity of the host rock, which is normally as resistive as 10^6 Ωm, but by the interconnectivity of the conductive fluid or melt in pore spaces or along grain boundaries, which can reduce the host resistivity to below 1 Ωm. Thus, the sensitivity of the electromagnetic method allows minor amounts of fluid, and the interconnectivity of fluids or melts in the crust and mantle, to be mapped. The transport of these minor amounts of fluid through the rock can also be estimated since the required connectivity must fit the low bulk resistivity of the rock.

Fluids play an important role in subduction systems (e.g., Iwamori 1998). Northeastern (NE) Japan can be classified as a typical subduction zone and is therefore a suitable test site for the study of fluid distributions. The dehydration of the subducting slab in the mantle wedge results in the upward migration of fluids, causing peridotite to be converted to serpentine, which may be detected as conductive anomalies. Fluids can also lower the melting point of peridotite and magmatic melts as well as fluids will be created and transported upward towards the crust (Kawamoto et al. 2012). The presence of fluid in the crust causes localized deformation and seis-

* Correspondence: oga@ksvo.titech.ac.jp
[1]Volcanic Fluid Research Center, Tokyo Institute of Technology, 2-12-1 Ookayama, Meguro, Tokyo 152-8551, Japan
Full list of author information is available at the end of the article

micity (Hasegawa et al. 2005; Ogawa and Honkura 2004).

The MT method has been used to detect the presence of fluids or melts in the crust. Electromagnetic induction studies of NE Japan have been performed since the 1950s and have used band-limited instruments. The 2-D models presented in the 1980s were primitive and showed lower crustal conductors in the back-arc (Ogawa et al. 1986; Ogawa 1987; Utada 1987). In the 2000s, wideband MT equipment and 2-D inversion methodologies allowed detailed 2-D crustal resistivity sections in seismogenic zones to be determined (Mitsuhata et al. 2001; Ogawa et al. 2001). These studies showed that zones of high seismic activity were associated with resistive zones underlain by mid-crustal conductors. The observations are consistent with a fault-valve model (Sibson et al. 1988; Sibson 2009). Mishina (2009) and Asamori et al. (2010) performed 2-D inversions on MT profile data and suggested the existence of sub-vertical conductors under Naruko volcano and surrounding regions (Figure 1). The present study considers the two previous profile datasets together with recent data recorded by grid-spaced MT sites. The objective of this research was to generate a 3-D resistivity model that is correlated with the distribution of volcanic and seismic activity around Naruko volcano, NE Japan.

Data acquisition

The present study area is located in the central region of the NE Japanese arc (Figure 1). The area now known as NE Japan was in the past located at the margin of the Eurasian continent and rifted apart during the opening of the Sea of Japan in the Miocene (Sato 1994). In the late Miocene (7 to 5 Ma), when the tectonic stress was close to neutral, large collapsed calderas with diameters of approximately 10 km were formed in the study area (Yoshida 2001; Yoshida et al. 2013). From the late Pleistocene (1 Ma to the present), the area has been subjected to tectonic east-west compression, resulting in active volcanism such as Naruko and Mukaimachi volcanoes in the study area, Onikobe caldera volcano located farther north, and Funagata-yama volcano located farther south.

This study includes 32 new MT sites and 45 sites from previous studies along profiles (Mishina 2009; Asamori et al. 2010). All data, new and old data, were obtained using a Phoenix MTU5 system (Phoenix Geophysics, Toronto, Canada) with periods ranging from 0.003 to 2,000 s. The new sites span the area to the south of Naruko volcano using a grid arrangement with approximately 5-km spacing designed to image the crust around Naruko volcano in three dimensions.

Figure 2 shows the distribution of apparent resistivity and phase from the determinant of impedance tensors

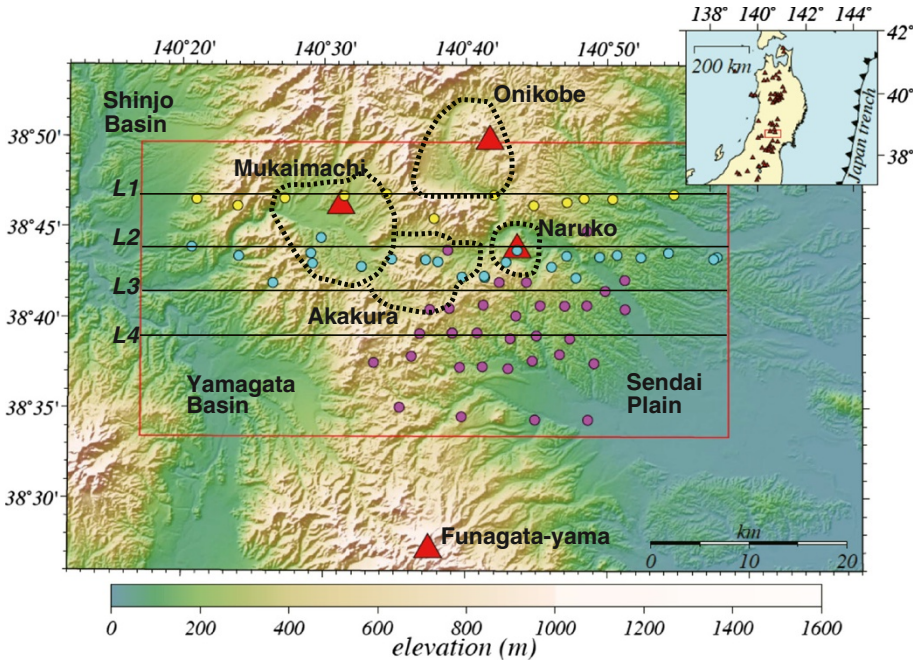

Figure 1 Study area in the northeastern Japan arc (inset map) and magnetotelluric sites around Naruko volcano. Purple dots denote new magnetotelluric sites used in this study. Yellow and blue dots denote magnetotelluric sites from previous studies by Mishina (2009) and Asamori et al. (2010), respectively. Major Quaternary volcanoes are shown by triangles. Late Miocene collapse calderas are outlined by dotted lines following Geological Survey of Japan (2013).

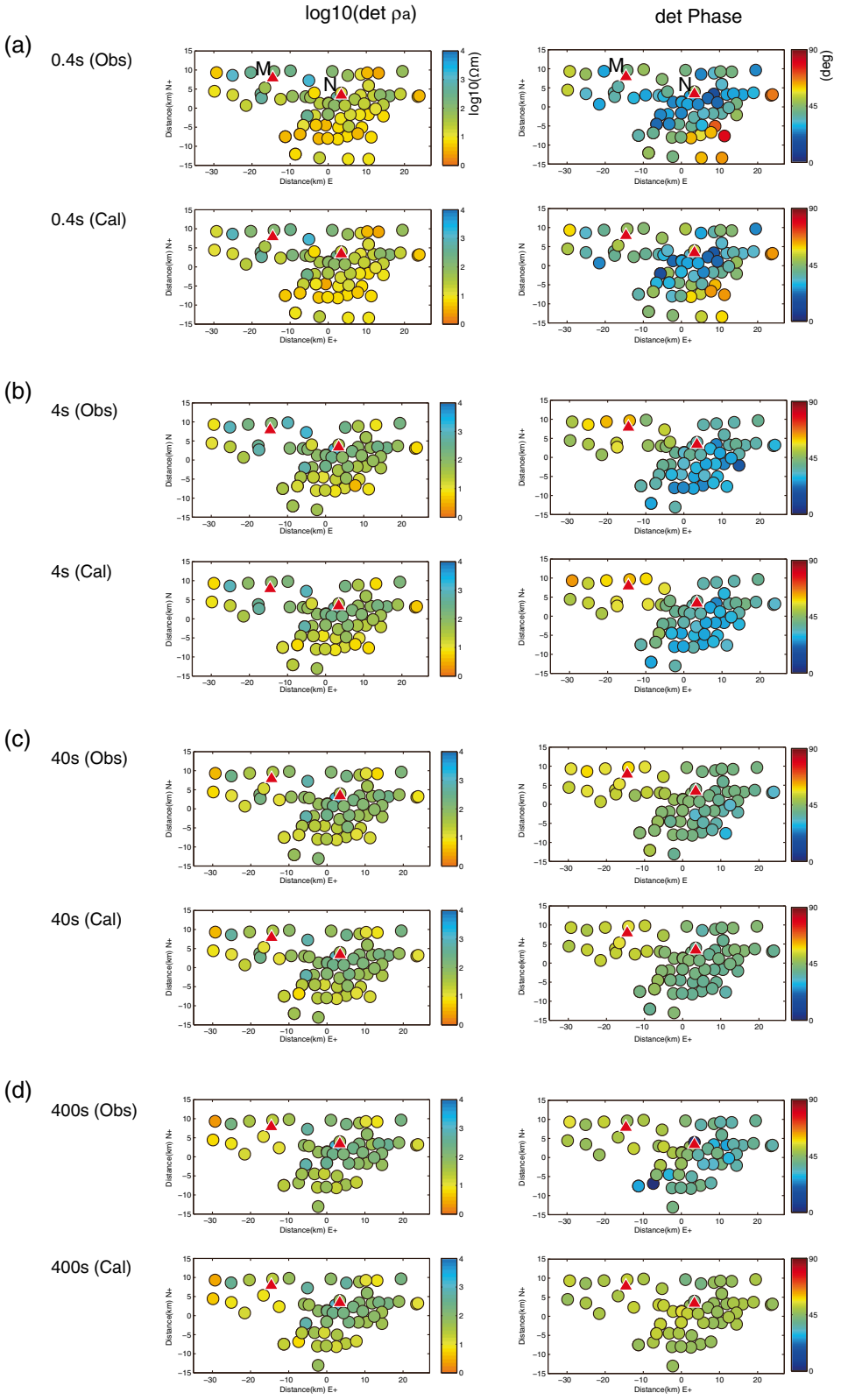

Figure 2 Apparent resistivity and phases from determinant of impedance tensors for four representative periods. (a) 0.4 s, **(b)** 4 s, **(c)** 40 s, and **(d)** 400 s. For each period, observed and calculated apparent resistivities and phases are shown by colored circles. The two triangles represent Naruko volcano in the east and Mukaimachi caldera in the west.

for the four representative periods (0.4 to 400 s). They are calculated as below:

$$\rho_a^{\mathrm{inv}} = \frac{|\det Z|}{\omega\mu}$$

$$\phi = \frac{1}{2}\tan^{-1}(\det Z)$$

These values do not depend on the coordinates, are rotation invariant, and are useful in understanding the general feature of the dataset, although the apparent resistivity may still be affected by the near-surface inhomogeneities. Observed low resistivities in the short period (yellow and orange circles in Figure 2a,b) correspond to the sedimentary layers of Sendai plain, Yamagata, and Shinjo basins (see Figure 1). As the period increases, Naruko volcano (N in the figure) is surrounded by resistive apparent resistivities (Figure 2c,d). However, the area around Mukaimachi caldera (M in the figure) to the west of Naruko volcano is surrounded by more conductive apparent resistivities. This basically corresponds to the existence of the major conductor between Naruko volcano (N) and Mukaimachi caldera (M), as we will show later. The determinant phases are also consistent with this feature. In the right column of Figure 2a, high determinant phases are evident at the southeastern corners of the map, corresponding to the sedimentary conductor of Sendai Plain. In the long periods (Figure 2b,c,d), high phases are getting evident to the west of Naruko volcano, implying an existence of the major conductor. All of the panels in Figure 2 also show respective model responses of the final model, which will be described later.

The phase tensor of the recorded dataset (Caldwell et al. 2004) is shown in the left column of Figure 3 at four representative periods. The phase tensor can graphically show the directionality and dimensionality of the dataset without being affected by local conductivity anomalies or any assumptions about 2-D structures. The upper and lower panels in Figure 3a show the phase tensor for the observed and calculated impedances at 0.4 s, respectively. The ellipse sizes are normalized by the maximum axis. The color bar represents the arithmetic average of $\tan^{-1}(\phi_{\min})$ and the $\tan^{-1}(\phi_{\max})$ of the phase tensor where the warmer colors indicate that the structures are more conductive. To prevent misleading conclusion from the poor-quality data, only good data with error of both off-diagonal impedance phases less than 10° were plotted. The shapes of the phase tensor ellipses are more circular than those with longer periods. Figure 3b shows the distribution of phase tensor ellipses at a period of 4 s. The colors and shapes of the phase tensor show more consistency between neighboring sites. The southern central sites show E-W elongated elliptical shapes, implying a N-S elongated resistive block surrounded by conductors (see R2 in Figure 4b,c,d). The distribution of phase tensor ellipses for the period of 40 s is shown in Figure 4c. In this figure, the shapes are more consistent and the thin ellipses align in a WNW-ESE orientation, suggesting the presence of a conductor with a NNE-SSW orientation. The suggested conductor follows the arc direction, as well as the coastline in the area. The model calculation described later in this paper also includes coastal effects from the Pacific Ocean and the Sea of Japan, but such thin ellipses were not explained without crustal conductors elongated NNE-SSW. We also observed changes in elliptic eccentricity at Naruko volcano where the ellipses are more circular towards the west and more elongated towards the east. Figure 3d shows the phase tensor ellipses for the period of 400 s. At this period, the colors and shapes of the ellipses exhibit a similar distribution to those for the period of 40 s.

The β values in phase tensor analyses were plotted in the right column in Figure 3, which represent three-dimensionality. The sites around Naruko volcano have large β values (Figure 3a). This is due to the shallow conductor located at Naruko volcano, which is surrounded by a more resistive upper crust. Towards longer periods, there are more sites with large β. At the periods of 40 and 400 s (Figure 3c,d), the high β values occupy the eastern part of the study area. This feature seems contradictory to the consistency of the distribution of the ellipses in the left column of Figure 3c,d. The cause of this feature will be discussed later.

3-D inversion

We used the 3-D inversion code by Siripunvaraporn and Egbert (2009), which had been parallelized for multiple frequencies. Full components of the impedance tensors for 77 sites were used in the inversion to produce 3-D resistivity structures. We selected eight periods of data, from 0.13 to 400 s in half-decade spacing. The horizontal mesh consisted of 1 × 1 km cells in the central core region (30 × 30 km), and the outer cells' sizes were gradually increased to cover 465 × 465 km. This mesh design allowed the coastal effect from both sides of the oceans, and from the Tsugaru Strait between Honshu and Hokkaido, to be incorporated. For vertical cells, the surface cells were 100 m in thickness and the thickness was increased with depth. The base of the cells was at a depth of 139 km. In total, 60 × 60 × 37 cells were used, including seven layers above ground.

The initial model assumed a uniform earth having a resistivity of 100 Ωm surrounded by ocean with a fixed resistivity of 0.25 Ωm. This initial model was also used as a prior model, and a smooth model was obtained using the Occam algorithm. The error floor of the

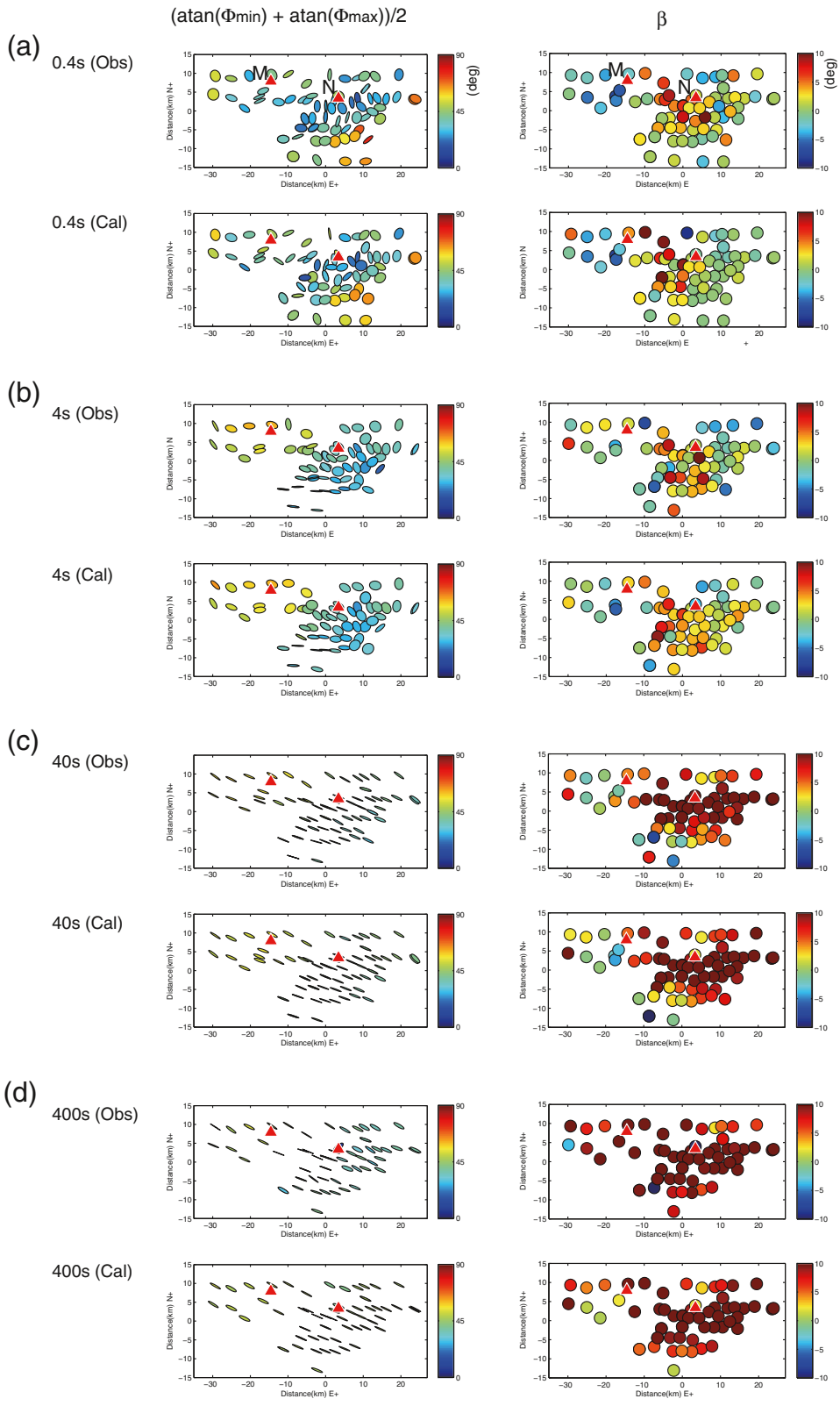

Figure 3 (See legend on next page.)

(See figure on previous page.)

Figure 3 Phase tensor ellipses (left column) and β (right column) for four representative periods. (a) 0.4 s, **(b)** 4 s, **(c)** 40 s, and **(d)** 400 s. For each period, observed and calculated phase tensor ellipses and β are shown for comparison. The size of each ellipse is normalized by the major axis. The color of each ellipse shows $\frac{1}{2}(\mathrm{atn}(\Phi\ \mathrm{min}) + \mathrm{atn}(\Phi\ \mathrm{max}))$. The two triangles represent Naruko volcano in the east and Mukaimachi caldera in the west.

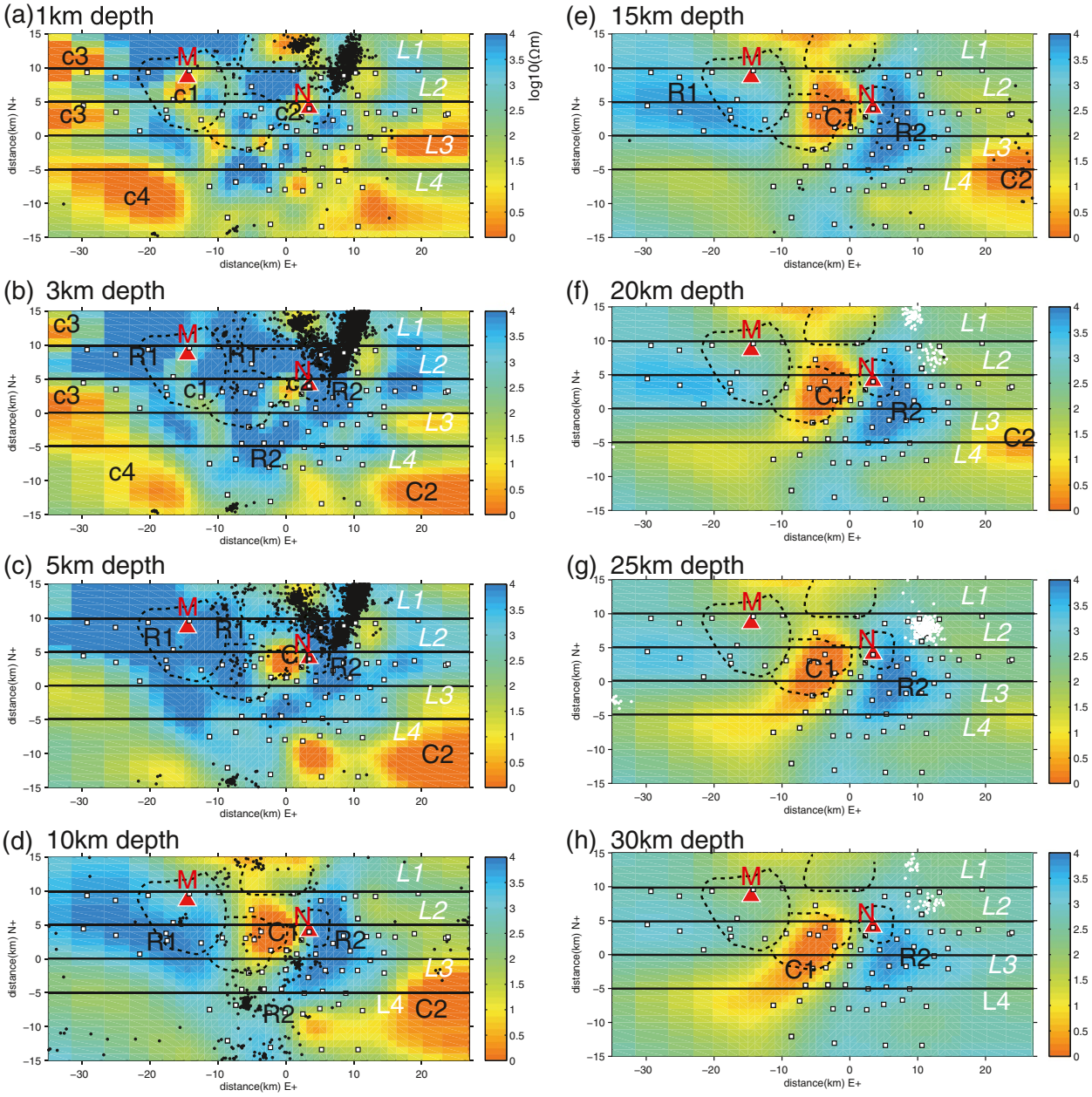

Figure 4 Resistivity depth sections for different depths. (a) 1 km, **(b)** 3 km, **(c)** 5 km, **(d)** 10 km, **(e)** 15 km, **(f)** 20 km, **(g)** 25 km, and **(h)** 30 km. The color denotes log10 (resistivity). The red triangles labeled N and M denote Naruko volcano and Mukaimachi caldera, respectively. The dotted line shows the outlines of the calderas as shown in Figure 1. The black and white dots represent hypocenters of normal earthquakes and long-period volcanic earthquakes at respective depths from the 1997 to 2011 JMA catalogue, respectively. The hypocenters were plotted with 2-km depth ranges for respective depths. Four east-west lines (L1 to L4) are profiles for the sections in Figure 5.

impedance was set at 10%. The RMS misfit was reduced to 3.12 after the fifth iteration. Here, we call this model as the first-generation model. This model was then used as an initial model and also as a new prior model for another series of iterative inversions. The fifth iteration gave a new model with minimum RMS of 1.87, and we take this as the second-generation model. In the same way, we had the third- and fourth-generation models with RMS of 1.63 and 1.60, respectively. As RMS is almost converged, we used the fourth-generation model as our final model. The near-surface telluric distortions were not explicitly incorporated into the model. We suggest that the resistivity of the model surface blocks accounts for static shift by producing contrasts between the adjacent sites.

The responses of the final model are shown as determinant apparent resistivity and phase (in Figure 2) and phase tensor ellipses and β (in Figure 3) for the representative periods. The observed and calculated responses generally fit well.

Results and discussion

Figure 4 shows representative depth sections. Each panel also shows the seismic hypocentral locations with a depth tolerance of 2 km from the 1997 to 2011 seismic catalogue compiled by the Japan Meteorological Agency. At depths of 1 and 3 km (Figure 4a,b, respectively), the distribution of resistivity is consistent with the surface geology. Conductors c1 and c2 are located at Naruko and Mukaimachi volcanoes, respectively, and represent caldera fill. Conductors c3 and c4 represent sedimentary layers of the Shinjo and Yamagata basins, respectively (Figure 1). Towards the southeastern edge of the model, conductor C2 is evident at a depth of 3 km but this area is not covered by the MT data and requires careful investigation before interpretation. The existence of C2 was confirmed by the sensitivity test as described later in the Appendix.

Structures at 5-km depth (Figure 4c) show more resistive features than those at shallower depths. At a depth of 10 km (Figure 4c), a conductor in 10-km diameter appears to the west of Naruko volcano. The seismicity at these depths is distributed in the resistive region, in particular R2, which is sandwiched between conductors C1 and C2.

Deeper structures (Figure 4e,f,g,h) show greater elongation of conductor C1 along the NNE-SSW direction, and the contrast with the eastern resistive block R2 is clearer. This direction is consistent with the 2-D strike direction determined by Asamori et al. (2010). The eastern conductor C2 disappears at depths below 25 km.

Long-period earthquakes at 20- to 30-km depth are shown in Figure 4f,g,h in white dots, and imply injections of magmatic melt into the crust, although their locations are distant from conductor C1 and Naruko volcano (approximately 10 km away). The long-period earthquakes are located at the edge of the resistive block R2 and are not associated with a significant conductive anomaly.

Resistivity sections for L1 to L4 in Figure 4 are shown in Figure 5. Profile L1 (Figure 4a) almost overlaps with one of the profiles shown by Mishina (2009). Although section L1 is oriented east-west and the corresponding profile (Mishina 2009) is rotated by 15° clockwise from the north, the geometry of the conductors is relatively consistent. We observe clearly defined clusters of earthquakes above conductor C1. The brittle-ductile transition is defined by the cutoff where the seismicity coincides with the top of conductor C1. Thus, we interpreted C1 not as a melt, but as a saline fluid reservoir. The conductive feature extends smoothly to the west; however, there is a sharp resistivity contrast between C1 and resistor R2 in the east. Farther to the east of resistor R2, there are clusters of long-period volcanic earthquakes (shown as white dots) in the lower crust.

Section L2 (Figure 4b) can be compared with that of Asamori et al. (2010). Figure 6a,b compares sections from 3-D and 2-D inversions using the same color scale. The sub-vertical conductor (C1) in the 3-D model has lower resistivity than the conductor (C1') in the 2-D model (Figure 6b). There are two possible reasons. One is the difference in treating the shallow galvanic effect. The 2-D model is inverted together with static shift as parameters (Ogawa and Uchida 1996), whereas the 3-D model assumes that the shallow blocks represent galvanic distortions including static shift. The other reason is that the 3-D structure has a finite strike length of approximately 10 km (Figure 4d,e,f,g,h). Lower resistivity is needed to produce strong inductive responses to account for a low apparent resistivity where the electric current flows along strike. In this 3-D model, we cannot expect enough charge buildup at the ends of the elongated C1 conductor, which may lower apparent resistivity (Ting and Hohmann 1981). We have also found that the crustal anomaly C' in the 2-D model disappeared in the 3-D model. This C' conductor in the 2-D model may be erroneous projection of an off-line sedimentary conductor.

The leading edge of the C1 conductor approaches the surface conductor c2, which is in the middle of Naruko caldera. The level of shallow seismicity is high along the profile, and the hypocenters are distributed in the resistive body surrounding the C1 conductor. The C1 conductor shows a pathway of saline fluid at depth to the surface. A helium isotope anomaly provides direct support for such supply from the upper mantle to Naruko volcano (Asamori et al. 2010; Horiguchi et al. 2010). Similar vertical conductors were also observed below

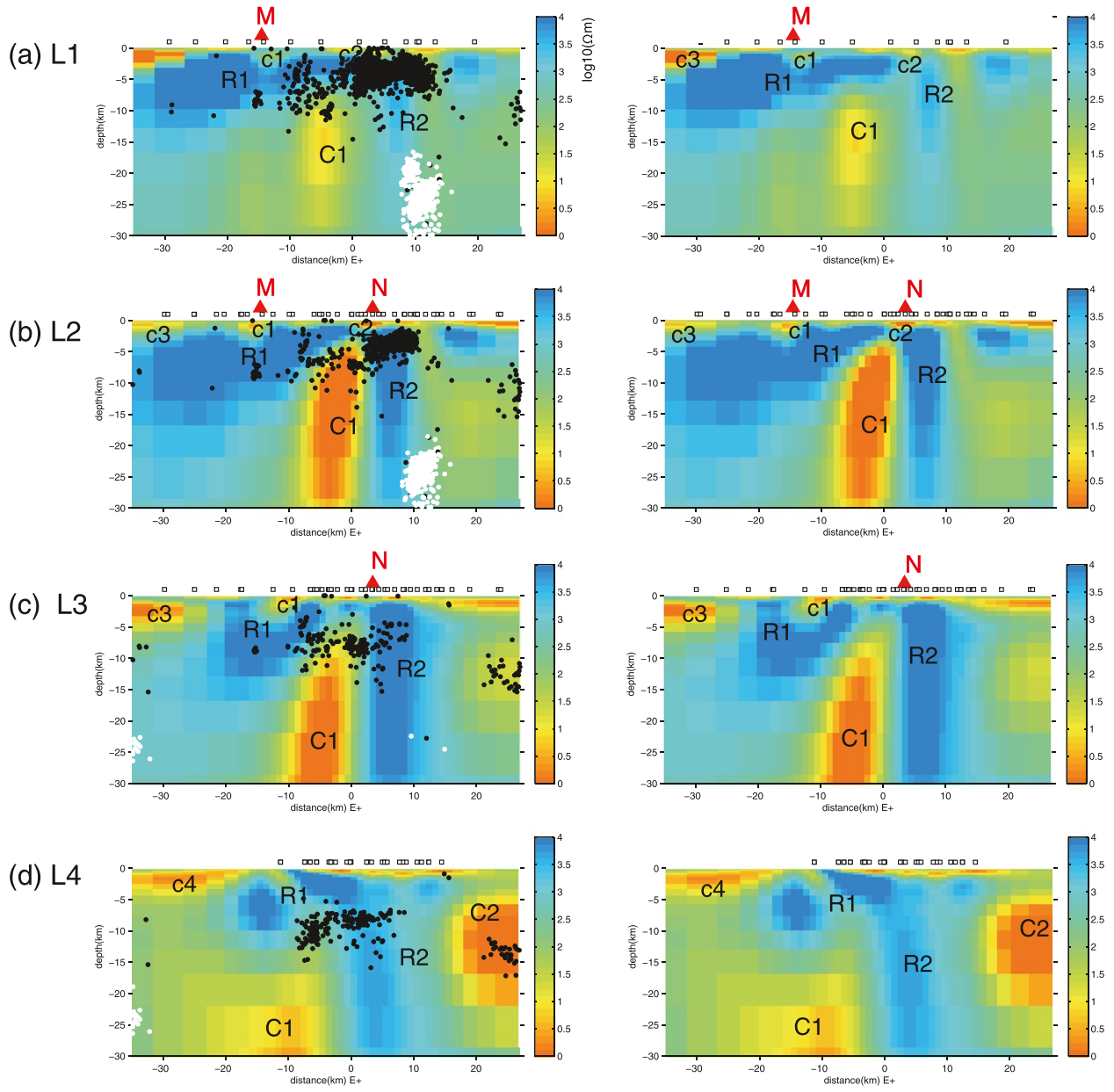

Figure 5 Resistivity sections for profiles L1 (a), L2 (b), L3 (c), and L4 (d) in Figure 4. Left and right columns show resistivity models with and without seismic hypocenters, respectively. The black and white dots indicate normal earthquakes and long-period volcanic earthquakes, respectively. The triangles on the surface denote Quaternary volcanoes. M and N indicate the locations of Naruko volcano and Mukaimachi caldera, respectively. Labels for the conductors and resistors correspond to those in Figure 4.

Onikobe caldera (Fukino 2011) to the north of the study area.

Section L3, oriented east-west and located 5 km south of Naruko volcano, shows that the top of the sub-vertical conductor (C1) is deeper and its resistivity is higher than those in Figure 3b. We also observed deeper hypocenters above the C1 conductor. Section L4, located 5 km farther south, is characterized by a more blurred and deeper C1 conductor. Correspondingly, the hypocenters are also deeper, being close to 15-km depth.

The mid- to lower crustal conductors in this study showed resistivities of 1 to 10 Ωm. As shown in Figure 5, the top of the sub-vertical conductor is directly below the hypocenters, i.e., just below the brittle-ductile transition. The existence of the conductor could imply the presence of saline fluids rather than magmatic melt, although these are not easily discriminated purely on the resistivity value alone. If we assume a fluid salinity, we can infer the minimum porosity, based on a fluid-bearing rock model such as Hashin-Shtrikman bounds

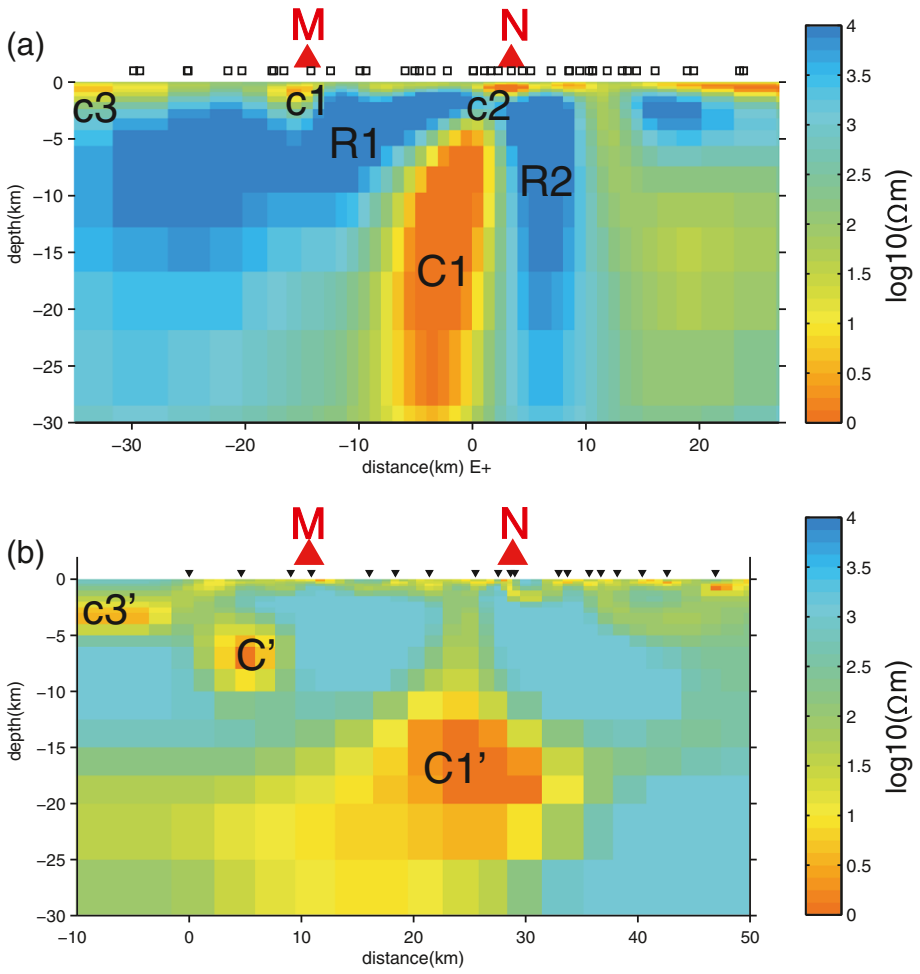

Figure 6 Comparison between (a) the 3-D model and (b) the 2-D model. 3D model along line L2 is compared with 2-D model (Asamori et al. 2010) with the same color scale. Major conductors are labeled.

(Hashin and Shtrikman 1962; Pommier and Le-Trong 2011). According to Nesbitt (1993), typical crustal fluids have resistivities of 0.01 to 1 Ωm. Recent mantle xenolith studies by Kawamoto et al. (2013) reported the salinity of fluids in the mantle wedge to be 5.1 wt%, which is more conductive than that of seawater, but the difference is by a factor of <10. Here, we made a first-order assumption that the fluid conductivity is 0.1 Ωm, which corresponds to four times as high salinity as that of seawater. The Hashin-Shtrikman bounds for the fully connected fluid case require a porosity of 1.5% to 15% for a conductive anomaly of 1 to 10 Ωm (Pommier and Le-Trong 2011). Recently, Shimojuku et al. (2014) also showed that fluid of high salinity (>10 wt%) is required to account for 10-Ωm bulk resistivity, from the resistivity measurement of fluid-bearing rocks under lower crustal conditions.

The resistivity sections can be compared with the seismic tomography results presented in Nakajima and Hasegawa (2003) and Okada et al. (2014). The sub-vertical conductor C1 below Naruko volcano corresponds to both Vp and Vs images that show low velocity anomalies (approximately 5%) from the lower crust to the surface. However, the lower part (>15-km depth) shows high Vp/Vs (>1.82), whereas the upper part (<15-km depth) shows low Vp/Vs (approximately <1.75). The lower part, which shows low Vp and Vs but high Vp/Vs, is interpreted as representing a partial melt. The upper part, which shows low Vp and Vs but low Vp/Vs, is interpreted as a zone of high fluid content (Nakajima and Hasegawa 2003; Okada et al. 2014). The lower solubility of quartz in the upper crust (Newton and Manning 2000) will create a sealing cap for the deeper fluid due to precipitated quartz. The reduced solubility of quartz in the upper crust may also contribute to the lower Vp/Vs ratio (Christensen 1996). Thus, our electrical image, as well as the seismic image, is consistent with quartz solubility controls on the distribution of saline fluid in the crust.

Conclusion

The 3-D resistivity structure was inverted from wide-band MT data recorded by 77 sites around Naruko volcano, NE Japan. Full-component impedance tensors at eight representative periods were used in the inversion, using a 100-Ωm uniform earth with surrounding ocean as the initial model. The model fit was quantified by RMS misfit and by mapping the observed and calculated phase tensor ellipses. The model showed a sub-vertical conductor C1 below Naruko volcano. The conductor showed a sharp contrast at the eastern border compared with a blurred western border. The depth to the conductor was shallow in the vicinity of Naruko volcano and increased towards the north and south. At a depth of ≥15 km, the conductor was elongated NNE-SSW. The crustal seismicity distribution showed a cutoff depth, consistent with the top of the conductor at depth. Near Naruko volcano, levels of shallow seismicity (<5 km) were high and were associated with the top of the sub-vertical conductor, which was close to the surface. This observation suggests that the crustal seismicity is fluid driven. The fluids are presumably supplied by a partial melting zone at a greater depth, and the top of the fluid reservoir is capped by a self-sealed precipitate of silicate solution at temperatures of approximately 400°C.

At greater crustal depths, the backbone ranges are associated with 2-D conductors elongated in the NNE-SSW direction. The Quaternary volcanic front is characterized by a sharp resistivity contrast and a high resistivity zone of 10- to 15-km width to the east. Farther

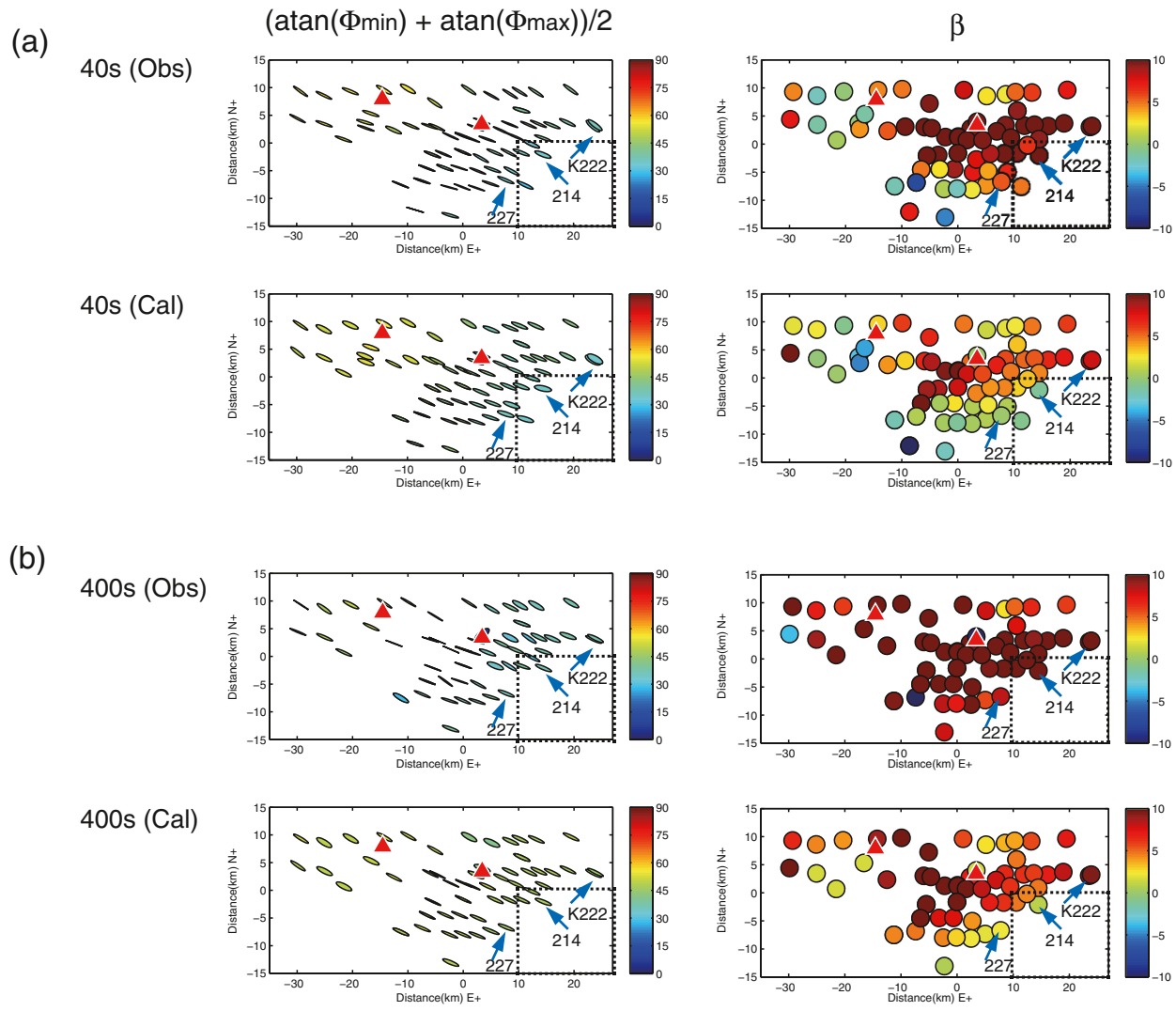

Figure 7 Phase tensor ellipse and *β* for sensitivity test for two representative periods. (a) 40 s and **(b)** 400 s. The dotted squares show the horizontal location of the area where the C2 conductor is replaced with 100 Ωm. The calculated *β* values of the sites west of the C2 conductor are significantly underestimated. We do not see significant differences with and without the C2 as seen in phase tensor ellipses; however, without the C2 conductor, the observed large *β* value to the west of the C2 is not explained.

to the east, a fore-arc conductor was observed in the mid-crust. This conductor did not have a deep root. The resistivity image is consistent with results from seismic tomography. The crustal conductors along-arc and in the fore-arc have resistivities of 1 to 10 Ωm. If we assume a Hashin-Shtrikman model using saline fluids of 0.1 Ωm, a porosity of 1.5% to 5% would be required to explain the bulk resistivity of 1 to 10 Ωm.

Further data acquisition and compilation of previous datasets are both underway, and the distribution of crustal fluids will be imaged for a larger area (Ichihara et al. 2014; Kanda and Ogawa 2014) together with seismic data (Okada et al. 2012; Okada et al. 2014).

Appendix

Sensitivity test of the C2 conductor

The existence of the C2 conductor in Figure 4 was tested by the forward modeling because the C2 conductor was outside the site coverage. The C2 anomaly was replaced by a 100-Ωm resistivity. The left column of Figure 7 shows the comparison of observed and calculated phase tensor ellipses for the periods of 40 and 400 s. The dotted square at the lower right corner shows the location of the C2 conductor. From the phase tensor shapes, we do not see any clear differences. However, the β values are very sensitive to C2. The calculated β near the C2 anomaly now have low values. Figure 8 shows typical MT sites in Figure 7. Final model responses and test model responses are shown by solid lines and broken lines, and observed responses are shown by symbols. At site K222 (Figure 8a), the off-diagonal phase curves (green solid and broken lines) differ significantly at periods longer than 40 s. The final model successfully explains phase over quadrant responses. The difference between final and model responses is clear in diagonal elements. The off-diagonal elements at site 227 (Figure 8b) are not very sensitive to C2, but the amplitudes of the diagonal elements are sensitive. The diagonal elements of site 214 (Figure 8c) are sensitive to C2 at periods longer than 40 s. These differences in sounding curves are easily seen in the map of β (Figure 7).

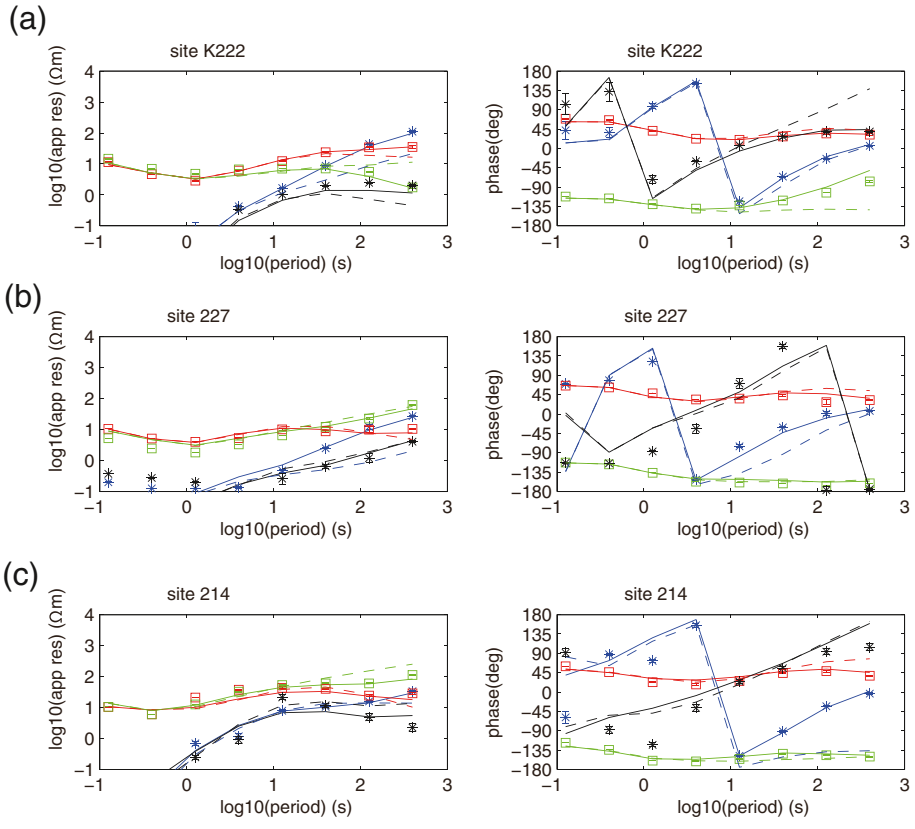

Figure 8 Sounding curves at three representative sites for sensitivity test with and without the C2 conductor. (a) Site K222. **(b)** Site 227. **(c)** Site 214. See Figure 7 for their locations. Blue, red, green, and black symbols with error bars (only where error bars are larger than the symbols) represent xx, xy, yx, and yy components, respectively. Those with solid lines and broken lines represent model responses with and without the C2 conductor, respectively.

Competing interests
The authors declare that they have no competing interests.

Authors' contributions
YO and MI designed the field survey for the new dataset. YO carried out the field survey, processed the time series data, performed the 3-D inversion, and drafted the manuscript. WK contributed to the inversion and compilation of some of the figures. MM and KA compiled the previous datasets. All authors read and approved the final manuscript.

Acknowledgements
We had fruitful discussions with E. Takahashi, T. Matsuzawa, T. Okada, H. Sakuma, M. Nakamura, H. Iwamori, H. Ichihara, and T.G. Caldwell. Comments from the two anonymous reviewers improved the manuscript. We thank W. Siripunvaraporn of Mahidole University for the WSINVMT3D code (Siripunvaraporn and Egbert 2009). Numerical calculations were carried out on TSUBAME 2.0 at the Global Scientific Information and Computing Center of the Tokyo Institute of Technology. Some figures were prepared using the Generic Mapping Tools (Wessel and Smith 1991). This study was supported by JSPS KAKENHI Grant Number 21109003. We used hypocenter data processed by the Japan Meteorological Agency with the Ministry of Education, Culture, Sports, Science and Technology. These data were provided by the National Research Institute for Earth Science and Disaster Prevention, Geographical Survey Institute, Hokkaido University, Hirosaki University, Tohoku University, University of Tokyo, Nagoya University, Kyoto University, Kochi University, Kyushu University, Kagoshima University, Japan Marine Science and Technology Center, National Institute of Advanced Industrial Science and Technology, Tokyo Metropolitan Government, Aomori Prefectural Government, Shizuoka Prefectural Government, Hot Springs Research Institute of Kanagawa Prefecture, and City of Yokohama.

Author details
[1]Volcanic Fluid Research Center, Tokyo Institute of Technology, 2-12-1 Ookayama, Meguro, Tokyo 152-8551, Japan. [2]Research Center for Prediction of Earthquakes and Volcanic Eruptions, Tohoku University, 6-6 Aoba, Aramaki, Aoba-ku, Sendai 980-8578, Japan. [3]Tono Geoscientific Research Unit, Geological Isolation Research and Development Directorate, Japan Atomic Energy Agency, 959-31, Jorinji, Izumi, Toki 509-5102, Japan.

Received: 4 April 2014 Accepted: 13 November 2014
Published online: 04 December 2014

References

Aizawa K, Koyama T, Hase H, Uyeshima M, Kanda W, Utsugi M, Yoshimura R, Yamaya Y, Hashimoto T, Yamazaki K, Komatsu S, Watanabe A, Miyakawa K, Ogawa Y (2014) Three-dimensional resistivity structure and magma plumbing system of the Kirishima volcanoes as inferred from broad-band magnetotelluric data. J Geophys Res 119:1–18, doi:10.1002/2013JB010682

Asamori K, Umeda K, Ogawa Y, Oikawa T (2010) Electrical resistivity structure and helium isotopes around Naruko volcano, northeastern Japan and its implication for the distribution of crustal magma. Int J Geophys 2010:1–7, doi:10.1155/2010/738139

Caldwell TG, Bibby HM, Brown C (2004) The magnetotelluric phase tensor. Geophys J Int 158:457–469, doi:10.1111/j.1365-246X.2004.02281.x

Christensen NI (1996) Poisson's ratio and crustal seismology. J Geophys Res 101:3139, doi:10.1029/95JB03446

Fukino (2011) Three-dimensional crustal resistivity structure around the Onikobe caldera revealed by magnetotellurics. Master thesis, Tokyo Institute of Technology, 64

Geological Survey of Japan (2013) Volcanoes of Japan, 3rd edn. Geological Survey of Japan, AIST, Tsukuba

Hasegawa A, Nakajima J, Umino N, Miura S (2005) Deep structure of the northeastern Japan arc and its implications for crustal deformation and shallow seismic activity. Tectonophysics 403:59–75, doi:10.1016/j.tecto.2005.03.018

Hashin Z, Shtrikman S (1962) On some variational principles in anisotropic and nonhomogeneous elasticity. J Mech Phys Solids 10:335–342

Hill GJ, Caldwell TG, Heise W, Chertkoff DG, Bibby HM, Burgess MK, Cull JP, Cas RAF (2009) Distribution of melt beneath Mount St Helens and Mount Adams inferred from magnetotelluric data. Nat Geosci 2:785–789, doi:10.1038/ngeo661

Horiguchi K, Ueki S, Sano Y, Takahata N, Hasegawa A, Igarashi G (2010) Geographical distribution of helium isotope ratios in northeastern Japan. Island Arc 19:60–70, doi:10.1111/j.1440-1738.2009.00703.x

Ichihara H, Sakanaka S, Mishna M, Uyeshima M, Nishitani T, Ogawa Y, Yamaya Y, Mogi T, Amita K, Miura T (2014) A 3-D electrical resistivity model beneath the focal zone of the 2008 Iwate-Miyagi Nairiku earthquake (M 7.2). Earth Planets Space 66:50

Ingham MR, Bibby HM, Heise W, Jones K, Cairns P, Dravitzki S, Bennie SL, Caldwell TG, Ogawa Y (2009) A magnetotelluric study of Mount Ruapehu volcano, New Zealand. Geophys J Int 179:887–904, doi:10.1111/j.1365-246X.2009.04317.x

Iwamori H (1998) Transportation of H_2O and melting in subduction zones. Earth Planet Sci Lett 160:65–80, doi:10.1016/S0012-821X(98)00080-6

Kanda W, Ogawa Y (2014) Three-dimensional electromagnetic imaging of fluids and melts beneath the NE Japan arc revisited by using geomagnetic transfer function data. Earth Planets Space 66:39, doi:10.1186/1880-5981-66-39

Kawamoto T, Kanzaki M, Mibe K, Matsukage KN, Ono S (2012) Separation of supercritical slab-fluids to form aqueous fluid and melt components in subduction zone magmatism. Proc Natl Acad Sci U S A 109:18695–18700, doi:10.1073/pnas.1207687109

Kawamoto T, Yoshikawa M, Kumagai Y, Mirabueno MHT, Okuno M, Kobayashi T (2013) Mantle wedge infiltrated with saline fluids from dehydration and decarbonation of subducting slab. Proc Natl Acad Sci U S A 110:9663–9668, doi:10.1073/pnas.1302040110

Mishina M (2009) Distribution of crustal fluids in northeast Japan as inferred from resistivity surveys. Gondwana Res 16:563–571, doi:10.1016/j.gr.2009.02.005

Mitsuhata Y, Ogawa Y, Mishina M, Kono T, Yokokura T, Uchida T (2001) Electromagnetic heterogeneity of the seismogenic region of 1962 M6.5 Northern Miyagi Earthquake, northeastern Japan. Geophys Res Lett 28:4371–4374

Nakajima J, Hasegawa A (2003) Tomographic imaging of seismic velocity structure in and around the Onikobe volcanic area, northeastern Japan: implications for fluid distribution. J Volcanol Geotherm Res 127:1–18, doi:10.1016/S0377-0273(03)00155-0

Nesbitt BE (1993) Electrical resistivities of crustal fluids. J Geophys Res 98:4301, doi:10.1029/92JB02576

Newton R, Manning C (2000) Quartz solubility in H_2O-NaCl and H_2O-CO_2 solutions at deep crust-upper mantle pressures and temperatures: 2–15 kbar and 500–900°C. Geochemica Cosmochem Acta 64:2993–3005

Ogawa Y (1987) Two-dimensional resistivity modelling based on regional magnetotelluric survey in the northern Tohoku district, northeastern Japan. J Geomagn Geoelectr 39:349–366

Ogawa Y, Honkura Y (2004) Mid-crustal electrical conductors and their correlations to seismicity and deformation at Itoigawa-Shizuoka Tectonic Line, Central Japan. Earth Planets Space 56:1285–1291

Ogawa Y, Uchida T (1996) A two-dimensional magnetotelluric inversion assuming Gaussian static shift. Geophys J Int 126:69–76

Ogawa Y, Yukutake T, Utada H (1986) Two-dimensional modelling of resistivity structure beneath the Tohoku district, northern Honshu Japan, by a finite element method. J Geomagn Geoelectr 38:45–79

Ogawa Y, Mishina M, Goto T, Satoh H, Oshiman N, Kasaya T, Takahashi Y, Nishitani T, Sakanaka S, Uyeshima M, Takahashi Y, Honkura Y, Matsushima M (2001) Magnetotelluric imaging of fluids in intraplate earthquake zones, NE Japan back arc. Geophys Res Lett 28:3741–3744

Okada T, Umino N, Hasegawa A (2012) Hypocenter distribution and heterogeneous seismic velocity structure in and around the focal area of the 2008 Iwate-Miyagi Nairiku Earthquake, NE Japan—possible seismological evidence for a fluid driven compressional inversion earthquake. Earth Planets Space 64:717–728, doi:10.5047/eps.2012.03.005

Okada T, Matsuzawa T, Nakajima J, Uchida N, Yamamoto M, Hori S, Kono T, Nakayama T, Hirahara S, Hasegawa A (2014) Seismic velocity structure in and around the Naruko volcano, NE Japan, and its implications for volcanic and seismic activities. Earth Planets Space 66:114, doi:10.1186/1880-5981-66-114

Pommier A, Le-Trong E (2011) "SIGMELTS": a web portal for electrical conductivity calculations in geosciences. Comput Geosci 37:1450–1459, doi:10.1016/j.cageo.2011.01.002

Sato H (1994) The relationship between Late Cenozoic tectonic events and stress field and basin development in northeast Japan. J Geophys Res 99:22261–22274

Shimojuku A, Yoshino T, Yamazaki D (2014) Electrical conductivity of brine-bearing quartzite at 1 GPa: implications for fluid content and salinity of the crust. Earth Planets Space 66:2, doi:10.1186/1880-5981-66-2

Sibson RH (2009) Rupturing in overpressured crust during compressional inversion—the case from NE Honshu, Japan. Tectonophysics 473:404–416, doi:10.1016/j.tecto.2009.03.016

Sibson RH, Robert F, Poulsen KH (1988) High-angle reverse faults, fluid-pressure cycling, and mesothermal gold-quartz deposits. Geology 16:551–555, doi:10.1130/0091-7613(1988)016

Siripunvaraporn W, Egbert G (2009) WSINV3DMT: vertical magnetic field transfer function inversion and parallel implementation. Phys Earth Planet Interiors 173:317–329

Ting SC, Hohmann GW (1981) Integral equation modeling of three-dimensional magnetotelluric response. Geophysics 46:192–197

Utada H (1987) A direct inversion method for two-dimensional modeling in the geomagnetic induction problem. PhD thesis, The University of Tokyo

Wannamaker PE, Caldwell TG, Jiracek GR, Maris V, Hill GJ, Ogawa Y, Bibby HM, Bennie SL, Heise H (2009) Fluid and deformation regime of an advancing subduction system at Marlborough, New Zealand. Nature 460:733–736, doi:10.1038/nature08204

Wessel P, Smith WHF (1991) Free software helps map and display data. EOS Trans 296 AGU 72:445–446

Yoshida T (2001) Late Cenozoic magmatism in the NE Japan arc. Earth Science (Chikyu Kagaku) 63:260–288 (in Japanese and English abstract)

Yoshida T, Kimura J-I, Yamada R, Acocella V, Sato H, Zhao D, Nakajima J, Hasegawa A, Okada T, Honda S, Ishikawa M, Prima ODA, Kudo T, Shibazaki B, Tanaka A, Imaizumi T (2013) Evolution of late Cenozoic magmatism and the crust-mantle structure in the NE Japan arc. Geol Soc London Spec Publ 385:335–387, doi:10.1144/SP385.15

doi:10.1186/s40623-014-0158-y
Cite this article as: Ogawa *et al.*: **Three-dimensional magnetotelluric imaging of crustal fluids and seismicity around Naruko volcano, NE Japan.** *Earth, Planets and Space* 2014 **66**:158.